Enhanced Purcell factor for nanoantennas supporting interfering resonances

Rémi Colom[1], Felix Binkowski[1], Fridtjof Betz[1], Yuri Kivshar[2,3], Sven Burger[1,4*]
[1] *Zuse Institute Berlin, Takustraße 7, 14195 Berlin, Germany*
[2] *Nonlinear Physics Center, Research School of Physics, Australian National University, Canberra ACT 2601, Australia*
[3] *ITMO University, St. Petersburg 197101, Russia and*
[4] *JCMwave GmbH, Bolivarallee 22, 14050 Berlin, Germany*

We study the effect of coupled resonances and quasi-bound states in the continuum (quasi-BICs) on the Purcell factor in dielectric resonant nanoantennas. We analyze numerically interfering resonances in a nanodisk *with* and *without* a substrate when the modes are coupled to an emitter localized inside the nanodisk, and we quantify the modal contributions to the Purcell factor also reconstructing the radiation patterns of the resonant system. It is revealed that the Purcell effect can be boosted substantially for a strong coupling of resonances in the quasi-BIC regime.

I. INTRODUCTION

Resonances play a central role in the control of light-matter interactions in nanophotonics. Plasmonic resonances enable such a control via large near-field enhancements [1, 2], which allows, e.g., for realizing plasmonic nanoantennas to tailor the radiation from quantum emitters [3, 4]. Recently, the excitation of Mie-type resonant modes in high-refractive-index dielectric resonators has proven to be very useful for a wide range of applications, from the enhancement of nonlinear effects to a resonant control of the phase in metasurfaces [5]. One important figure of merit for measuring the effect of resonances on light-matter interactions is their quality factor (*Q-factor*), that quantifies the ability of a structure to trap light and to enhance the electromagnetic fields.

Nanoresonators act as nanoantennas for strongly localized light sources, like quantum dots or defects in crystalline lattices, which can allow for the realization of efficient single-photon sources by enhancing the emission of light [6, 7]. Such a control of the emission via the modification of the electromagnetic environment is a concept that dates back to the pioneering work of Purcell [8] performed in the microwave range followed by the experiments of Drexhage [9] that demonstrated the possibility of controlling the lifetime of fluorescent molecules in the visible range. This phenomenon is ubiquitous, and it has also been used to control the resonant scattering by dielectric nanorod antennas [10].

The figure of merit that quantifies the emission enhancement is called *the Purcell factor* [8], and it is proportional to the Q-factor. Optical nanoantennas were first realized with plasmonic materials [3, 4], but recently dielectric resonators have been shown to allow for large enhancements of the Purcell factor via the excitation of both electric and magnetic optically-induced Mie-type resonances [11]. The excitation of magnetic resonances presents the advantage of enhancing light emission also via the magnetic dipole transitions. This effect was first theoretically predicted [11–13] and confirmed later in experiments [14–16]. This is a very promising application for dielectric nanoantennas as the enhancement of light emission empowered by the magnetic dipole resonances is an emerging area of research [17, 18]. The enhancement of the Purcell factor was used successfully to improve the emission of quantum dots in silicon nanoantennas [19] and also for metallic and hybrid nanoantennas [20]. Control of the emission can also be achieved dynamically [21]. Finally, nanoantennas can also be designed to enhance the performance of quantum emitters, providing promising platforms for the realization of single-photon sources [22].

Bound states in the continuum (BICs) appear as a special type of nonradiating modes associated with an infinite Q-factor [23]. Such states can originate from different physical mechanisms [24, 25]. Symmetry protected BICs occur in photonic crystal slabs, and they result from the impossibility of these modes to couple to propagating fields outside the photonic crystal because of symmetry restrictions [23, 26]. Further, the so-called accidental BICs appear from interferences between several resonances [23, 24]. They are observed when a system parameter is varied continuously. This concept was introduced in quantum mechanics where the coupling between resonances is controlled by engineering the potential [27].

In optics, one of the first attempts to study BICs was made in the physics of photonic crystals [28]. While BICs can be realized in gratings or photonic crystals which are infinite in two directions, it is much more challenging to observe such BICs in compact structures and even more in subwavelength systems [23]. The existence of BICs, also called *embedded eigenstates*, was predicted theoretically in a coated nanosphere where the permittivity of the outer shell vanishes [29]. In more realistic configurations, it is still possible to take

* Correspondence email address: burger@zib.de

advantage of the coupling of resonances in nanostructures to increase the Q-factor of one resonance, even if it does not lead to accidental BICs with infinite Q-factors. In photonics, such an approach was suggested to enhance the Q-factors of the modes of optical microcavities [30] and coupled dielectric nanopillars [31]. It was shown recently that high-refractive index nanodisks supporting multiple resonances are a good platform to employ this approach [32–34]. Due to similarity of this approach with accidental BICs [27], the large Q-factors achieved through the interference of several resonances are called *quasi-BICs*. Quasi-BICs have been observed experimentally in AlGaAs nanodisks [35], and they have been used in various applications [24, 36] including nonlinear optics [37–39] and lasing from a single nanoparticle [40].

Unlike BICs, which lead to a perfect confinement of light, quasi-BICs suffer from residual radiation losses. As a consequence, for a rigorous treatment of quasi-BICs it is important to use quasinormal modes (QNMs) and associated complex eigenfrequencies which generalizes modal approaches to dissipative and non-Hermitian systems [41–43]. The influence of quasi-BICs on light-matter interactions and, in particular, their coupling to a light source can be quantified by using QNM expansions. The QNM analysis of the coupling of an electromagnetic dipole source to an optical resonator, i.e., the modal expansion of the Purcell factor, has been carried out through several approaches [11, 44–47].

In this paper, we study quasi-BICs numerically. We consider dielectric nanoresonators either *with* or *without* a substrate and demonstrate that they can support interfering resonances with a strong coupling between a pair of modes. We carry out numerical simulations with a localized source embedded into the resonator to demonstrate different physical regimes. Modal expansions of the Purcell factor and far-field patterns reveal a complex interplay between different modal contributions interfering destructively in the spectral vicinity of quasi-BICs, yielding a strong enhancement of the Purcell factor and single modal excitation when the parameters of the source and resonator are tuned to match the quasi-BIC conditions.

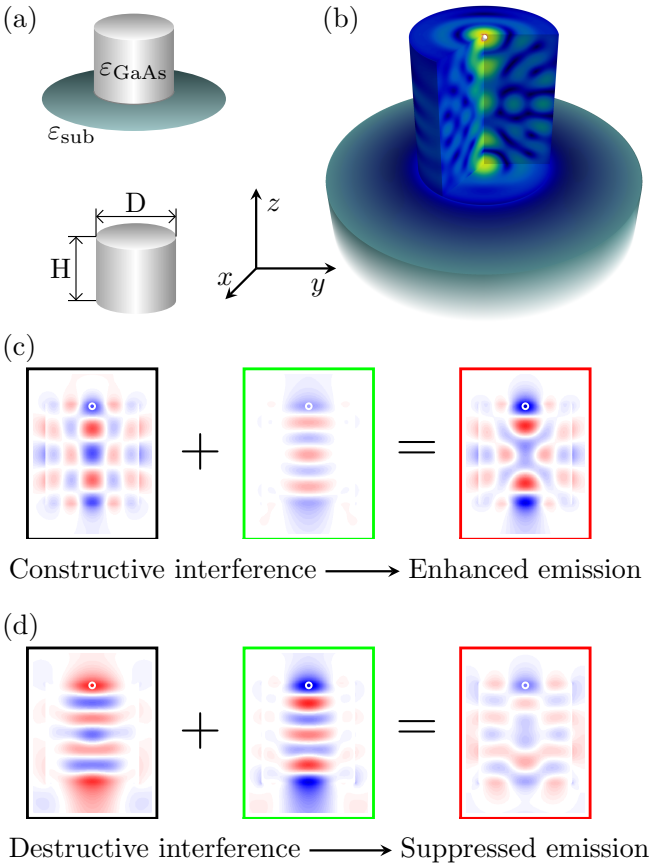

Figure 1. Principle of the enhanced and suppressed emission with interfering resonances. (a) Schematics of GaAs nanodisks with and without a substrate. The aspect ratio D/H is tuned to control the interference between the two main modes of the nanodisk. (b) Visualization of the electromagnetic field distribution resulting from a dipole emitter, represented by a white sphere, which is located below the top face of the nanodisk. Its frequency is chosen to excite the two modes of interest. (c) and (d): 2D cross-sections through the dominant two modal fields (left) and the total field distribution (right) visualizing the real part of the y field component. Red and blue colors correspond to negative and positive fields, respectively. The emitter position is indicated with a white circle. (c) When the two modal fields are excited in phase they interfere constructively, leading to enhancement of dipole emission. (d) Out-of-phase excitation of the two modal fields at a different dipole emission frequency, results in suppressed emission.

The major steps followed in this article are illustrated in Fig. 1. In Sec. II, we vary the aspect ratio D/H of a GaAs nanodisk to control the interference between the two modes of the nanodisk with or without a substrate. In particular, the strong coupling between these modes leads to the appearance of a high-Q mode: the quasi-BIC resonance. Sec. III considers the coupling of a dipole source with the nanodisk, leading to a complex electromagnetic response as seen in Fig. 1(b). Modal expansions are employed to analyze the role of the interference between the nanodisk modes for the coupling with the dipole. These expansions enable to identify how the constructive interference between two modal contributions leads to the enhancement of the dipole emission, as illustrated in Fig. 1(c). On the other hand, destructive interference leads to the inhibition of the dipole emission, as illustrated in Fig. 1(d). The modal analysis of the radiation pattern is carried out in Sec. IV. Finally, Sec. V concludes the paper.

II. QUASI-BICS IN ISOLATED NANODISKS

To understand the appearance of quasi-BIC states, first we review the theoretical approach employed to study the mode coupling [30, 48, 49]. A good insight in the physics of strong coupling for interfering resonances can be gained from a phenomenological model of mode coupling that involves the two modes with the uncoupled eigenfrequencies $\omega_{\mathrm{un},1}$ and $\omega_{\mathrm{un},2}$. When these two eigenfrequencies are far apart in the complex plane, there is no coupling between them. However, when the eigenfrequencies get close to each other, the coupling has to be taken into account and modifies the trajectories of these eigenfrequencies when a parameter is varied. The eigenfrequencies of the coupled modes can be found as the eigenvalues of an effective two-mode Hamiltonian, and they are equal to

$$\omega_{\pm} = \left(\frac{\omega_{\mathrm{un},1} + \omega_{\mathrm{un},2}}{2}\right) \pm \sqrt{\gamma},$$

where

$$\gamma = \left(\frac{\omega_{\mathrm{un},1} - \omega_{\mathrm{un},2}}{2}\right)^2 + v^2$$

with v being the coupling coefficient between the modes [48]. We are interested in the regime where these two resonances are close to each other, and therefore we assume that $\mathrm{Re}\,(\omega_{\mathrm{un},1}) = \mathrm{Re}\,(\omega_{\mathrm{un},2})$ and v is real as in Ref. [48].

As explained in [30, 48], two regimes of the mode coupling may be realized depending on the relation between v and $\frac{1}{2}(\omega_{\mathrm{un},1} - \omega_{\mathrm{un},2})$. When $2v < |\,\mathrm{Im}\,(\omega_{\mathrm{un},1} - \omega_{\mathrm{un},2})\,|$, the mode eigenvalues become

$$\omega_{\pm} = \left(\frac{\omega_{\mathrm{un},1} + \omega_{\mathrm{un},2}}{2}\right) \pm i\sqrt{|\gamma|},$$

and one observes that the coupling mostly alters the imaginary part of the eigenvalues resulting in an avoided crossing of the imaginary parts of the coupled eigenvalues and a crossing of their real parts. This behavior is a direct signature of the mode weak coupling. On the other hand, if $2v > |\,\mathrm{Im}\,(\omega_{\mathrm{un},1} - \omega_{\mathrm{un},2})\,|$, the mode eigenvalues are presented as

$$\omega_{\pm} = \left(\frac{\omega_{\mathrm{un},1} + \omega_{\mathrm{un},2}}{2}\right) \pm \sqrt{|\gamma|},$$

suggesting that the coupling of the eigenmodes mostly alters the real part of the eigenfrequencies yielding, this time, an avoided crossing of the real parts of the coupled eigenvalues and a crossing of the imaginary parts. In the

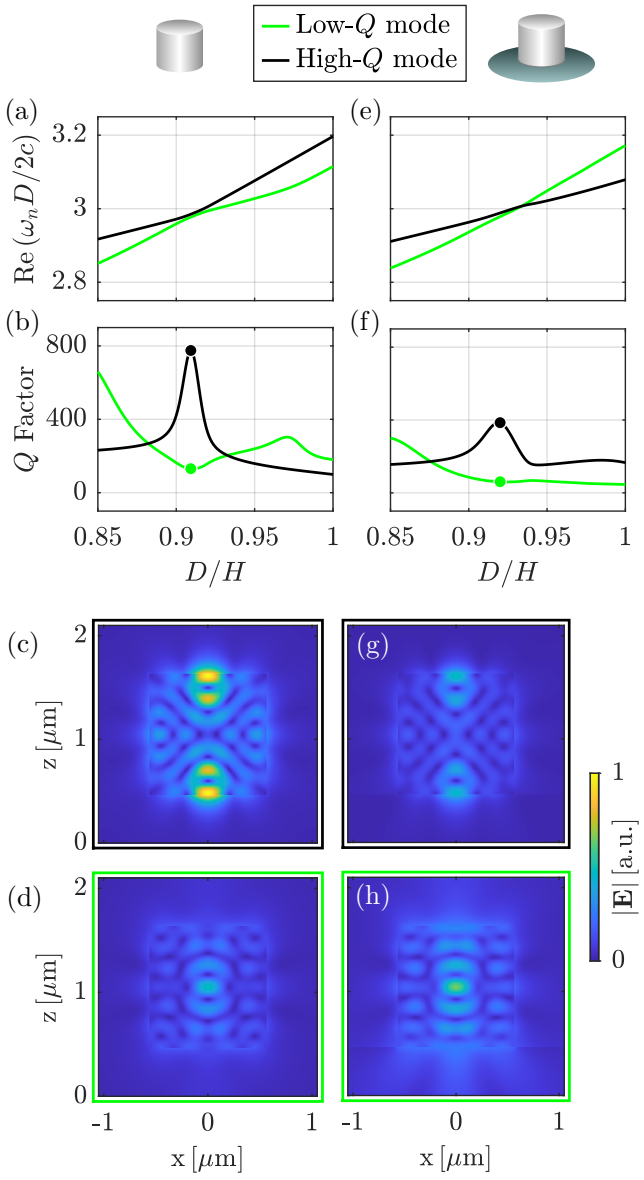

Figure 2. Real parts of two eigenfrequencies of interest (a, e) and corresponding Q-factors (b, f) as function of nanodisk aspect ratio D/H. Avoided crossing of the real parts and local maximum and minimum of the Q-factors at $D/H = 0.909$ indicate strong coupling for the nanodisk *without* substrate (a, b). Crossing of the real parts of two eigenfrequencies at $D/H = 0.93$ and avoided crossing of the Q-factor curves at $D/H = 0.944$ leading to a peak at $D/H = 0.92$ indicate weak coupling for the nanodisk *with* substrate (e, f). Field intensity maps $|\mathbf{E}|$ of the QNMs in an $x-z$-cross section through the 3D field distribution. (c), resp. (d), corresponds to the high-Q (resp. low-Q) mode of the isolated nanodisk [at the aspect ratio indicated by the black, resp. green, dot in (b)]. (g), resp. (h), corresponds to the high-Q (resp. low-Q) mode of the nanodisk with substrate [black, resp. green, dot in (f)].

following, we discuss how the mode coupling may result in the appearance of a hybridized quasi-BIC mode.

We consider a Gallium Arsenide (GaAs) nanodisk resonator with a height $H = 1260\,\text{nm}$ and varying diameter D in two different configurations: The nanodisk is just surrounded by air (case 1), and, the nanodisk is placed on a glass substrate and surrounded by a superspace of air (case 2). The optical properties of the system are investigated in the near-infrared wavelength range; the corresponding constant relative permittivities in our model are $\varepsilon_{\text{GaAs}} = 11.56$, $\varepsilon_{\text{sub}} = 2.25$, and $\varepsilon_{\text{air}} = 1.0$. The time-harmonic optical fields are modeled using Maxwell's equations,

$$\nabla \times \mu_0^{-1} \nabla \times \mathbf{E}(\mathbf{r}, \omega) - \epsilon(\mathbf{r}) \omega^2 \mathbf{E}(\mathbf{r}, \omega) = i\omega \mathbf{J}(\mathbf{r}), \quad (1)$$

where μ_0 is the vacuum permeability, $\epsilon(\mathbf{r})$ is the permittivity, and $\mathbf{J}(\mathbf{r})$ the source current density. For numerically solving Eq. (1), we use an adaptive, higher-order finite element method (FEM) [50]. For computing the eigenmodes $\mathbf{E}_n$ of the system and their associated eigenfrequencies ω_n, i.e., solutions to Eq. (1) where $\mathbf{J} = 0$, the cylindrical symmetry of the system is taken into account. Only modes with an azimuthal quantum number equal to 1 or -1 are investigated because these are the only ones excited by a dipole located on the axis of rotation, which is the configuration we are investigating in the second part of this study.

In order to find a quasi-BIC condition, the interference between two modes of the structure has to be tuned [30, 32, 51]. This is done by varying the geometry parameter, D, and computing eigenmodes $\mathbf{E}_n$ and their associated eigenfrequencies ω_n, where n is the mode index. Note that alternatively, a perturbation approach based on QNMs may be employed for finding the quasi-BICs [52]. Figure 2(a,b,e,f) shows how the normalized frequency, $\text{Re}(\omega_n D/2c)$, and the Q-factor,

$$Q = -\frac{1}{2} \frac{\text{Re}(\omega_n)}{\text{Im}(\omega_n)},$$

depend on the aspect ratio D/H. In Fig. 2(a,b), the case where the GaAs nanodisk is located in air is considered. It can be observed that the real part of the eigenfrequencies is showing a repulsion behavior at $D/H = 0.909$ and an almost coinciding peak reaching $Q \approx 800$ is observed for the Q-factor of one of the modes while a minimum is seen for the other mode. As discussed above, this behavior is an indication of strong coupling between the two modes. The high-Q mode can thus be considered to be a quasi-BIC. Figures 2(e,f) show the results for the second case, where the nanodisk is put on a glass substrate. It can be observed that, for the investigated modes and parameter range, the real part of the eigenfrequencies shows a crossing at $D/H = 0.933$. We observe a peak of the Q-factor reaching $Q \approx 400$ at $D/H = 0.92$. In fact, this peak is linked to the anti-crossing or level-repulsion occurring for the imaginary parts of the eigenfrequencies. This avoided crossing of the imaginary parts of the eigenfrequencies shows up in Fig. 2(f) at about $D/H = 0.944$. The qualitative analysis based on the effective Hamiltonian discussed above shows that this behavior is an indication of weak coupling between the two modes. The transition from strong to weak coupling when a substrate is added indicates that there must be an exceptional point, i.e., a condition for which the two coupled eigenvalues would become degenerated [53], when continuously varying the refractive index of the substrate from 1 to 1.5 [48, 49, 54, 55]. To conclude the discussion on the avoided crossing of the eigenfrequencies, we show, in Figs. 2(c,d,g,h), the field patterns associated with both modes when the Q-factor is maximized. For the case without substrate, this occurs for $D/H = 0.909$ while, when the substrate is added, the maximum occurs for an aspect ratio of $D/H = 0.92$. This helps to understand the level repulsion observed since, in both cases, the modes have apparently very different field patterns: The high-Q mode field is concentrated in hot spots located at the top and bottom of the disk while, for the low-Q mode, it is concentrated at the center of the disk. This apparent difference in the localization of the modes certainly prevents their merging.

III. COUPLING OF A POINT SOURCE TO A NANORESONATOR

Now, we turn to the study of a dipole emitter coupled to the investigated nanoresonator considering the two cases, the nanoresonator with and without substrate. It is worth noting that the coupling of a dipole with a BIC in an array of nanoparticles have already been studied [56], but we will here focus on the coupling of a dipole with the quasi-BIC arising in an individual nanodisk. We consider Maxwell's equations, given by Eq. (1), with the current density $\mathbf{J} = \mathbf{j}\delta(\mathbf{r} - \mathbf{r}_\text{d})$ that is a point source located at $\mathbf{r}_\text{d}$. The Purcell factor, which is used to quantify the enhancement of the emission, is defined as $\Gamma(\omega) = -[\text{Re}(\mathbf{E}(\omega, \mathbf{r}_\text{d}) \cdot \mathbf{j}^*(\omega, \mathbf{r}_\text{d}))]/[2\Gamma_\text{b}(\omega)]$, where $\Gamma_\text{b}(\omega)$ describes the emission of the dipole in a homogeneous medium of the permittivity ε_s. The interest of studying the Purcell factor and its modal analysis is twofold. On the one hand, one can see how a mode with a Q-factor as large as the one of the quasi-BIC can affect the dipole emission. On the other hand, looking at the modal analysis of the Purcell factor would allow to use it as a probe to study the interplay between several modes. This is particularly interesting for quasi-BICs since interferences between modes are at the origin of their formation.

To do so, we start by considering the Purcell factor for a dipole located at the maximum of the field amplitude

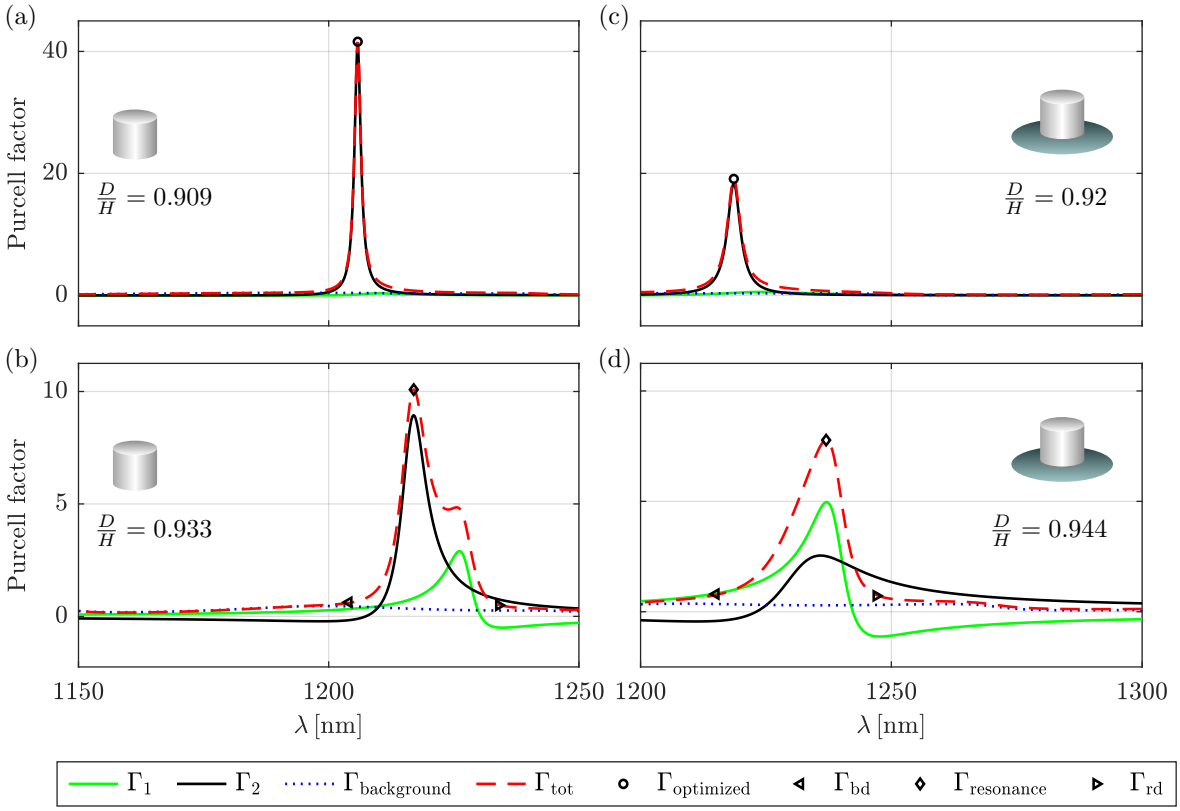

Figure 3. Modal analysis of the wavelength (λ) dependent Purcell factor Γ for a y-polarized dipole located on the symmetry axis 20 nm and 27 nm below the top face of the nanodisk in the case without substrate (a,b) and with substrate (c,d), respectively. (a) Modal expansion for the aspect ratio $D/H = 0.909$ (maximum Q-factor in Fig. 2(b). The high-Q mode corresponds to the modal Purcell factor Γ_2 (a black solid curve) and is solely responsible for the peak of the total Purcell factor Γ_{tot} (dashed red curve) at around 1205 nm. The contributions of the low-Q mode Γ_1 (green solid curve) and of the background $\Gamma_{\text{background}}$ (dotted blue line) are negligible. (b) Modal expansion for $D/H = 0.933$ (crossing of Q-factors in Fig. 2(b). Both modal terms Γ_1 and Γ_2 are of the same order of magnitude and destructively interfere in regions where they are of different sign. The impact of $\Gamma_{\text{background}}$ is constant and negligible in resonant regions. (c) Modal expansion for $D/H = 0.92$ (peak of the high Q-factor in Fig. 2(f). The high-Q mode corresponds to Γ_2 and is responsible for the peak of Γ_{tot} at around 1220 nm. (d) Modal expansion for $D/H = 0.944$ (avoided crossing of Q-factors in Fig. 2(f). The modal terms interfere, as in (b). The markers $\Gamma_{\text{optimized}}$, Γ_{bd}, $\Gamma_{\text{resonance}}$ and Γ_{rd} indicate the wavelengths for which far-field patterns are displayed in Fig. 4.

of the high-Q mode. This position is on the symmetry axis of the nanodisk, about 30 nm below the top face.

The consequences of the interplay between resonances at the origin of the quasi-BIC can be better understood by carrying out a modal analysis of the Purcell factor. Our method for deriving modal expansions relies on the use of Riesz projections [47, 57]. The modal expansion of the Purcell factor reads as

$$\Gamma(\omega) = \sum_{n=1}^{2} \Gamma_n(\omega) + \Gamma_{\text{background}}(\omega), \qquad (2)$$

where Γ_n are the modal contributions to the Purcell factor that are computed using contour integrals around the eigenfrequencies. Here, we take into account only the two interfering modes, i.e., the modes which are also shown in Fig. 2. The modal Purcell factors Γ_1 and Γ_2 are contributions corresponding to these two modes. The term $\Gamma_{\text{background}}$ contains the contributions of all other poles as well as the nonresonant background [47, 57]. Finally, Γ_{tot} corresponds to the total expansion including both the modal and background contributions. The different black markers indicate the wavelengths at which the radiation patterns are computed in Fig. 4. Details about the modal expansions are provided in supplemental material.

First, we look at the coupling of the dipole to the nanoresonator with the geometry corresponding to the maximum of the Q-factor in Fig. 2. The results of the modal analysis of the Purcell factor are displayed in Fig. 3(a), for a nanodisk in air with an aspect ratio

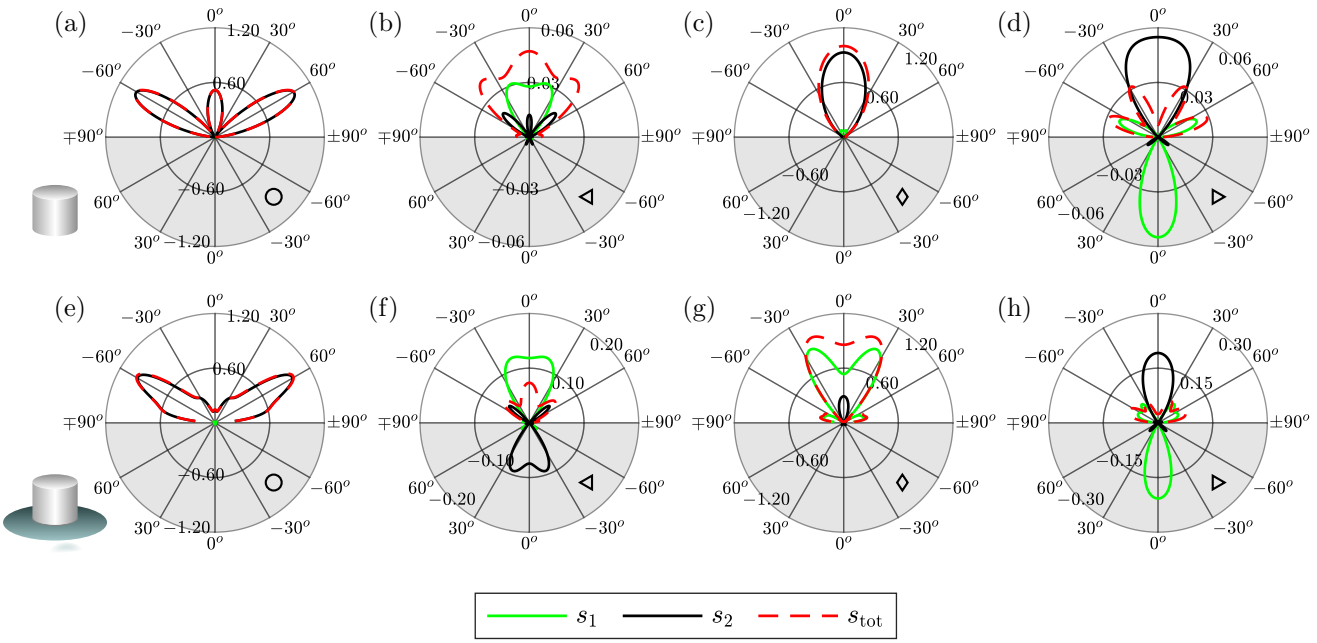

Figure 4. Modal decomposition of the θ-dependent, normalized radiation patterns towards the top for a dipole on the symmetry axis 20 nm and 27 nm below the top face of the nanodisk in the case without substrate (a-d) and with substrate (e-h), respectively. The green (black) solid curve corresponds to the angle-resolved, far-field modal energy flux s_1 (s_2) corresponding to the low-Q (high-Q) mode. The red dashed curve corresponds to the total energy flux s_{tot}. The upper half of each diagram shows positive contributions while the lower half in gray shows negative contributions. The dipole emission wavelengths correspond to the different Γ markers in Fig. 3 which are reproduced in the right bottom of each emission diagram. (a, e) show the on-resonant far field radiation for nanodisks supporting the quasi-BIC ($D/H = 0.909$ and $\lambda = 1206$ nm, resp. $D/H = 0.92$ and $\lambda = 1219$ nm) with clearly dominating contribution from the high-Q mode. (b-d), resp. (f-h) show the far field radiation for nanodisks with aspect ratios of $D/H = 0.933$, resp. $D/H = 0.944$ (i.e., at the avoided crossing, resp. crossing of the eigenfrequencies, cf., Figs. 2(a, e) for on-resonant sources ($\lambda = 1217$ nm/1237 nm in c/g) and off-resonant sources ($\lambda = 1204$ nm/1234 nm/1219 nm/1247 nm in b/d/f/h). While for on-resonant sources a single mode is predominantly contributing to the far field pattern (c, g), in off-resonant settings, the two relevant modes can interfere constructively (b) or destructively (d, f, h), as can be seen from the equal or different signs of the two dominant modal contributions in each case.

$D/H = 0.909$, and, in Fig. 3(c), for a nanodisk on a substrate with an aspect ratio $D/H = 0.92$. In both cases, the peak observed in the Purcell factor spectrum can be directly linked to the modal contribution corresponding to the high-Q mode. In the region around the peak, the contributions from the low-Q mode and the background are very small or even negligible. This demonstrates that, for a resonator supporting a quasi-BIC, an emitter may easily excite nearly exclusively this resonance. We note that the quasi-BIC allows to reach a high Purcell factor of $\Gamma \approx 40$ in the case without substrate and $\Gamma \approx 20$ in the case with substrate.

It is also worth looking at configurations where one can expect that the contributions to the Purcell factor from the two main modes would be of the same order of magnitude. This would allow us to investigate the interplay between modal contributions. This is the reason for showing, in Fig. 3(b), the Purcell factor for an aspect ratio of $D/H = 0.933$ for the disk without substrate corresponding to the crossing of the Q-factor of the two modes in Fig. 2(b). For the case with substrate, we consider the aspect ratio $D/H = 0.944$ as it corresponds to the avoided crossing of the imaginary parts of the eigenvalues as can be seen from the Q-factor trajectories in Fig. 2(f). This avoided crossing is caused by the interference of the interacting modes. Therefore, we expect that the interference will be seen in the contributions of the modal expansion. The Purcell factor again shows a distinct maximum, with a value of $\Gamma \approx 8$ with substrate and $\Gamma \approx 10$ without substrate. However, as expected, both modal contributions have the same order of magnitude. Also, the qualitative shape of both spectra of the modal Purcell factors are approximately mirror-symmetric to each other with respect to the resonance wavelength. This behavior yields the fact that, away from the resonance, the signs of the modal contri-

butions of the two modes are opposite, leading to destructive interference in these spectral regions. This is the case in Fig. 3(b) for wavelengths below $\sim 1210\,\mathrm{nm}$ and above $\sim 1230\,\mathrm{nm}$. For the case including a substrate in Fig. 3(d), we observe a similar behavior for wavelengths below $\sim 1225\,\mathrm{nm}$ and above $\sim 1245\,\mathrm{nm}$. The destructive interference between modes has been used previously to qualitatively describe the appearance of quasi-BICs [36]. In the present study, we show that the effect can be quantified by using modal expansion techniques.

IV. MODAL ANALYSIS OF RADIATION PATTERNS

It is well known that the coupling with nanostructures can alter the radiation pattern of a quantum emitter [3]. This ability to control the emission pattern of a dipole emitter with nanostructures has a great practical interest since it can improve the collection of the emitted field with an optical system. A modal analysis allows to understand how each mode but also the interferences between modes modifies the emission pattern. We will consider the far-field pattern of the energy flux density defined as $s(\mathbf{r},\omega) = \frac{1}{2}\,\mathrm{Re}\left(\mathbf{E}^*(\mathbf{r},\omega)\times\frac{1}{i\omega\mu_0}\nabla\times\mathbf{E}(\mathbf{r},\omega)\right)\cdot\mathbf{n}$, i.e., the projection of the Poynting vector on the normal vector $\mathbf{n}$ in the direction of field propagation. The modal expansion of $s(\mathbf{r},\omega)$ is computed using Riesz projections [57, 58] leading to the expression $s(\mathbf{r},\omega) = \sum_{n=1}^{2} s_n(\mathbf{r},\omega) + s_{\mathrm{background}}(\mathbf{r},\omega)$, where $\mathbf{r}$ is a point located in the far-field. We will in particular look at the dependency of the radiation pattern with θ in the x-z plane. In Fig. 4, the field patterns radiated by the dipole upwards towards the air are plotted for different wavelengths and for different aspect ratios. In Figs. 4(a-d), results are shown for the nanodisk without substrate for aspect ratios equal to 0.909 and 0.933 while Figs. 4(g-h) display results for the nanodisk on a substrate for aspect ratios equal to 0.92 and 0.944. Please note that the lower region of the plot shown in gray does not correspond to the field radiated downwards but to the negative modal contributions. Negative contributions are particularly important here, since, as for the Purcell factor, they are linked to the interferences between different modal contributions. Radiation pattern towards the substrate are actually shown in the supplemental material. In Figs. 4(a,e), we show the radiation pattern and its modal expansion at the aspect ratio and wavelength of the quasi-BIC. Just like for the Purcell factor, one mode has a much larger Q-factor than the other, it is not surprising to find that the radiation pattern can then be almost entirely understood from the contribution of the high-Q mode while the contributions from the low-Q mode is negligible compared to the contribution of the high-Q mode. The results of the modal expansion of the radiation pattern for the nanodisk without substrate with the aspect ratio equal to 0.933 are plotted in Figs. 4(b-d). These computations are made for the wavelengths on both sides of the main peak in Fig. 3(b), with 1204 nm, 1217 nm, and 1234 nm in Figs. 4(b, d), respectively.

For $\lambda = 1204\,\mathrm{nm}$, we obtain a positive contribution for both the modes summing up to a radiation lobe between $\sim \pm 45°$. For $\lambda = 1217\,\mathrm{nm}$, the main contribution is from mode 2 leading to a quite directional emission between $\sim \pm 30°$. Eventually, for $\lambda = 1234\,\mathrm{nm}$, an interference between the two main modal contributions is observed with a positive contribution from mode 2 between $\pm 30°$ and a negative contribution of mode 1 in the same range. In Figs. 4(f-h), we show the results of the modal expansions for the nanodisk on substrate with $D/H = 0.944$ for the wavelengths 1215 nm, 1237 nm, and 1247 nm, respectively. In Fig. 4(f), for $\lambda = 1215\,\mathrm{nm}$, the mode 1 has a positive contribution for angles between roughly 30 and -30 degrees while the mode 2 has a negative contribution in the same range of angles. Consequently, the total radiation pattern is suppressed, resulting from the interference between several modes. A very analogous behavior is observed at $\lambda = 1247\,\mathrm{nm}$ in Fig. 4(h), however, in this case, the mode 1 has a negative contribution while the mode 2 has a positive contribution. There is, again, a strong interference between the two modes and the far-field pattern cannot be understood without taking this interference into account. Finally, in Fig. 4(g), for $\lambda = 1237\,\mathrm{nm}$ corresponding to the peak of the Purcell factor in Fig. 3(b), we observe that the contribution from both modes of interest add up leading to a larger amplitude of the radiation by the dipole and to a confined far-field pattern.

V. CONCLUSION

We have numerically analyzed dielectric nanodisk resonators which support multiple resonances in overlapping frequency ranges. Using a finite-element-method-based framework, regimes where the resonators support quasi-BIC resonances have been investigated. The impact of the resonances on the Purcell factor describing the emission enhancement of a localized source has been shown in the quasi-BIC regime as well as in adjacent parameter regimes where several competing resonances are excited. The modal contributions to the Purcell factor have been computed using the Riesz projection method, and it has been shown that a single QNM causes the strongly enhanced dipole emission in the quasi-BIC situation. Further, we have investigated the modal, angular resolved far-field spectrum in on-resonance as well as off-resonance con-

ditions. This demonstrated that modal interference strongly impacts both, far-field emission strength as well as angular resolved radiation patterns. It has been shown that micron-scale dielectric resonators supporting quasi-BICs allow for high Purcell enhancement as well as for highly directed emission of light. We expect that, apart from the gained insight in the complex interference behavior in multi-modal resonators, these findings will allow for the design of efficient and robust future photonic components, such as single-photon emitters for quantum technology applications.

ACKNOWLEDGMENTS

The authors acknowledge funding from the German Research Foundation (DFG, Excellence Cluster MATH+, EXC-2046/1, project 390685689), the Helmholtz Association (Helmholtz Excellence Network SOLARMATH, a strategic collaboration of MATH+ and Helmholtz-Zentrum Berlin, project ExNet-0042-Phase-2-3), and the German Federal Ministry of Education and Research (BMBF Forschungscampus MODAL, project 05M20ZBM). Also, this project has received funding from the EMPIR program co-financed by the Participating States and by the European Union's Horizon 2020 research and innovation program (project 20FUN02 "POLIGHT"). Y.K. acknowledges support from the Australian Research Council (grants DP200101168 and DP210101292) and from the Russian Science Foundation (grant 21-72-30018).

[1] S. A. Maier and H. A. Atwater, J. Appl. Phys. **98**, 10 (2005).
[2] S. A. Maier, *Plasmonics: Fundamentals and Applications* (Springer Science & Business Media, 2007).
[3] L. Novotny and N. Van Hulst, Nat. Photonics **5**, 83 (2011).
[4] L. Novotny and B. Hecht, *Principles of nano-optics* (Cambridge University Press, 2012).
[5] A. I. Kuznetsov, A. E. Miroshnichenko, M. L. Brongersma, Y. S. Kivshar, and B. Luk'yanchuk, Science **354**, aag2472 (2016).
[6] I. Aharonovich, S. Castelletto, D. A. Simpson, C.-H. Su, A. D. Greentree, and S. Prawer, Rep. Prog. Phys. **74**, 076501 (2011).
[7] P. Lodahl, S. Mahmoodian, and S. Stobbe, Rev. Mod. Phys. **87**, 347 (2015).
[8] E. M. Purcell, Phys. Rev. **69**, 681 (1946).
[9] K. Drexhage, J. Lumin. **1**, 693 (1970).
[10] A. L. Holsteen, S. Raza, P. Fan, P. G. Kik, and M. L. Brongersma, Science **358**, 1407 (2017).
[11] X. Zambrana-Puyalto and N. Bonod, Phys. Rev. B **91**, 195422 (2015).
[12] B. Rolly, B. Bebey, S. Bidault, B. Stout, and N. Bonod, Phy. Rev. B **85**, 245432 (2012).
[13] M. K. Schmidt, R. Esteban, J. Sáenz, I. Suárez-Lacalle, S. Mackowski, and J. Aizpurua, Opt. Express **20**, 13636 (2012).
[14] M. Sanz-Paz, C. Ernandes, J. U. Esparza, G. W. Burr, N. F. van Hulst, A. Maitre, L. Aigouy, T. Gacoin, N. Bonod, M. F. Garcia-Parajo, *et al.*, Nano Lett. **18**, 3481 (2018).
[15] A. Vaskin, S. Mashhadi, M. Steinert, K. E. Chong, D. Keene, S. Nanz, A. Abass, E. Rusak, D.-Y. Choi, I. Fernandez-Corbaton, *et al.*, Nano Lett. **19**, 1015 (2019).
[16] H. Sugimoto and M. Fujii, ACS Photonics **8**, 1794–1800 (2021).
[17] S. Karaveli and R. Zia, Phys. Rev. Lett. **106**, 193004 (2011).
[18] D. G. Baranov, R. S. Savelev, S. V. Li, A. E. Krasnok, and A. Alù, Laser Photonics Rev. **11**, 1600268 (2017).
[19] V. Rutckaia, F. Heyroth, A. Novikov, M. Shaleev, M. Petrov, and J. Schilling, Nano Lett. **17**, 6886 (2017).
[20] A. Barreda, S. Hell, M. Weissflog, A. Minovich, T. Pertsch, and I. Staude, J. Quant. Spectrosc. Radiat. Transf. **276**, 107900 (2021).
[21] B. Casabone, C. Deshmukh, S. Liu, D. Serrano, A. Ferrier, T. Hümmer, P. Goldner, D. Hunger, and H. de Riedmatten, Nat. Commun. **12**, 1 (2021).
[22] A. S. Zalogina, R. Savelev, E. V. Ushakova, G. Zograf, F. Komissarenko, V. Milichko, S. Makarov, D. Zuev, and I. Shadrivov, Nanoscale **10**, 8721 (2018).
[23] C. W. Hsu, B. Zhen, A. D. Stone, J. D. Joannopoulos, and M. Soljačić, Nat. Rev. Mater. **1**, 16048 (2016).
[24] K. Koshelev, A. Bogdanov, and Y. Kivshar, Sci. Bull. **64**, 836 (2019).
[25] P. Tonkaev and Y. Kivshar, JETP Lett. **112**, 615 (2020).
[26] J. Lee, B. Zhen, S.-L. Chua, W. Qiu, J. D. Joannopoulos, M. Soljačić, and O. Shapira, Phys. Rev. Lett. **109**, 067401 (2012).
[27] H. Friedrich and D. Wintgen, Phys. Rev. A **32**, 3231 (1985).
[28] C. W. Hsu, B. Zhen, J. Lee, S.-L. Chua, S. G. Johnson, J. D. Joannopoulos, and M. Soljačić, Nature **499**, 188 (2013).
[29] F. Monticone and A. Alu, Phys. Rev. Lett. **112**, 213903 (2014).
[30] J. Wiersig, Phys. Rev. Lett. **97**, 253901 (2006).
[31] Q. Song and H. Cao, Phys. Rev. Lett. **105**, 053902 (2010).
[32] M. V. Rybin, K. L. Koshelev, Z. F. Sadrieva, K. B. Samusev, A. A. Bogdanov, M. F. Limonov, and Y. S. Kivshar, Phys. Rev. Lett. **119**, 243901 (2017).

[33] A. A. Bogdanov, K. L. Koshelev, P. V. Kapitanova, M. V. Rybin, S. A. Gladyshev, Z. F. Sadrieva, K. B. Samusev, Y. S. Kivshar, and M. F. Limonov, Adv. Photonics **1**, 016001 (2019).
[34] K. Koshelev and Y. Kivshar, ACS Photonics **8**, 102 (2020).
[35] E. Melik-Gaykazyan, K. Koshelev, J.-H. Choi, S. S. Kruk, A. Bogdanov, H.-G. Park, and Y. Kivshar, Nano Lett. **21**, 1765 (2021).
[36] K. Koshelev, A. Bogdanov, and Y. Kivshar, Opt. Photonics News **31**, 38 (2020).
[37] L. Carletti, K. Koshelev, C. De Angelis, and Y. Kivshar, Phys. Rev. Lett. **121**, 033903 (2018).
[38] L. Carletti, S. S. Kruk, A. A. Bogdanov, C. De Angelis, and Y. Kivshar, Phys. Rev. Res. **1**, 023016 (2019).
[39] K. Koshelev, S. Kruk, E. Melik-Gaykazyan, J.-H. Choi, A. Bogdanov, H.-G. Park, and Y. Kivshar, Science **367**, 288 (2020).
[40] V. Mylnikov, S. T. Ha, Z. Pan, V. Valuckas, R. Paniagua-Domínguez, H. V. Demir, and A. I. Kuznetsov, ACS Nano **14**, 7338 (2020).
[41] P. Lalanne, W. Yan, K. Vynck, C. Sauvan, and J.-P. Hugonin, Laser Photonics Rev. **12**, 1700113 (2018).
[42] P. T. Kristensen, K. Herrmann, F. Intravaia, and K. Busch, Adv. Opt. Photonics **12**, 612 (2020).
[43] T. Wu, M. Gurioli, and P. Lalanne, ACS Photonics **8**, 1522 (2021).
[44] C. Sauvan, J.-P. Hugonin, I. Maksymov, and P. Lalanne, Phys. Rev. Lett. **110**, 237401 (2013).
[45] R.-C. Ge, P. T. Kristensen, J. F. Young, and S. Hughes, New J. Phys. **16**, 113048 (2014).
[46] E. A. Muljarov and W. Langbein, Phys. Rev. B **94**, 235438 (2016).
[47] L. Zschiedrich, F. Binkowski, N. Nikolay, O. Benson, G. Kewes, and S. Burger, Phys. Rev. A **98**, 043806 (2018).
[48] C.-H. Yi, J. Kullig, M. Hentschel, and J. Wiersig, Photonics Res. **7**, 464 (2019).
[49] W. Heiss, Phys. Rev. E **61**, 929 (2000).
[50] J. Pomplun, S. Burger, L. Zschiedrich, and F. Schmidt, Phys. Status Solidi B **244**, 3419 (2007).
[51] L. Huang, L. Xu, M. Rahmani, D. Neshev, and A. E. Miroshnichenko, Adv. Photonics **3**, 016004 (2021).
[52] W. Yan, P. Lalanne, and M. Qiu, Phys. Rev. Lett. **125**, 013901 (2020).
[53] W. Heiss, J. Phys. A **45**, 444016 (2012).
[54] S. R.-K. Rodriguez, Eur. J. Phys. **37**, 025802 (2016).
[55] Z.-L. Deng, F.-J. Li, H. Li, X. Li, and A. Alù, arXiv preprint arXiv:2109.10533 (2021).
[56] D. R. Abujetas and J. A. Sánchez-Gil, Nanomaterials **11**, 998 (2021).
[57] F. Binkowski, F. Betz, R. Colom, M. Hammerschmidt, L. Zschiedrich, and S. Burger, Phys. Rev. B **102**, 035432 (2020).
[58] F. Betz, F. Binkowski, and S. Burger, SoftwareX **15**, 100763 (2021).

SUPPLEMENTAL MATERIAL

RIESZ PROJECTION PRINCIPLE AND RESULTS

Our approach for carrying out modal expansions relies on Riesz projections [47, 57, 58]. In a first step, the quantity of interest at real frequencies ω_0 is expressed as a contour integral using Cauchy's integral formula. To this end, it has to be analytically continued to the complex frequency plane. In a second step, the resonance expansion is obtained by deforming the contour around ω_0 until it encloses neighboring poles of the physical system and by the application of Cauchy's residue theorem. Each summand of the expansion corresponds to a contour integral, as illustrated in Fig. 6. The large contour accounts for poles outside the contour and for a nonresonant background.

Using the example of the Purcell factor $\Gamma(\omega_0) = -\frac{1}{2}\,\mathrm{Re}\left(\mathbf{E}(\omega_0, \mathbf{r}_d) \cdot \mathbf{j}^*(\omega_0, \mathbf{r}_d)\right)/\Gamma_b(\omega_0)$, whose expansion is shown in Fig. 3, the first step yields

$$\Gamma(\omega_0) = -\frac{1}{2\Gamma_b(\omega_0)} \oint_{C_0} \frac{\mathrm{Re}\left(\mathbf{E}(z, \mathbf{r}_d) \cdot \mathbf{j}^*(z, \mathbf{r}_d)\right)}{z - \omega_0} dz,$$

where C_0 is a contour around ω_0. The second step results in the desired expansion of the Purcell factor,

$$\Gamma(\omega_0) = \sum_n \Gamma_n(\omega_0) + \Gamma_{\text{background}}(\omega_0),$$

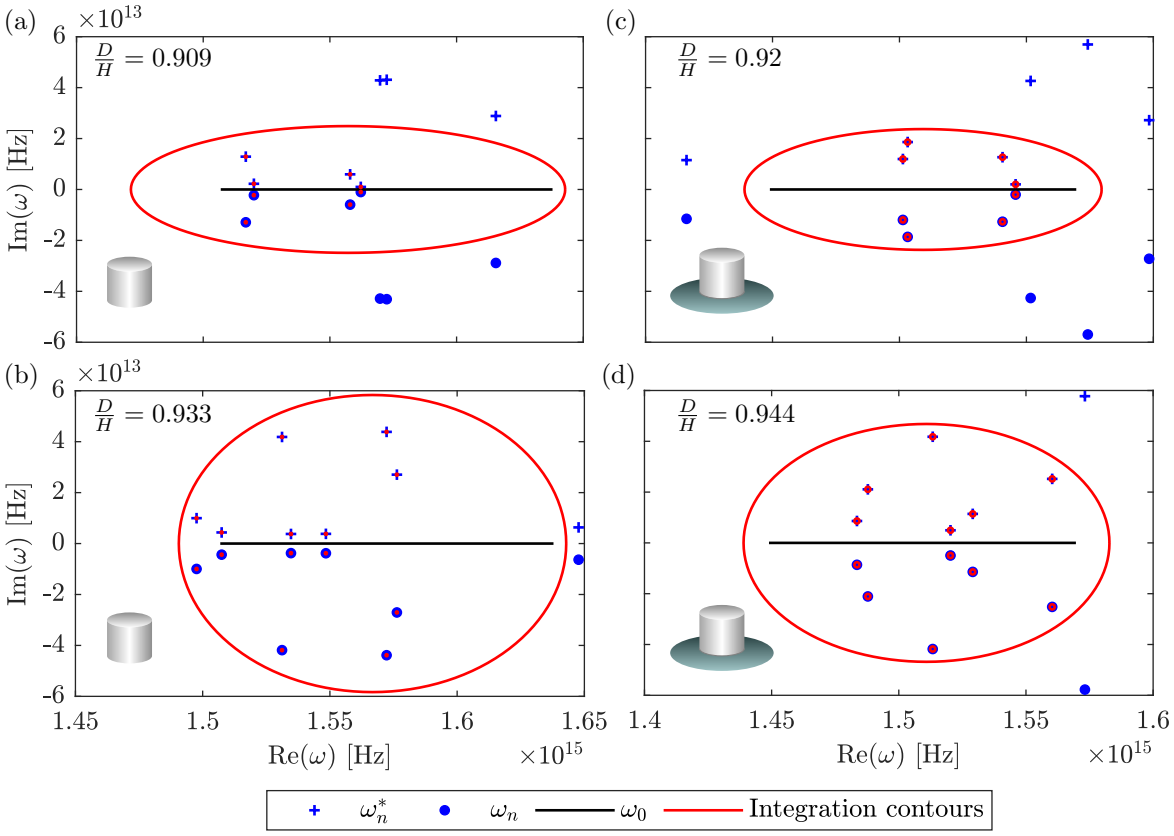

Figure 5. Contours used for the modal expansions of Purcell factor and emission pattern of a nanodisk with different aspect ratios D/H, either isolated or placed on a substrate. While the emission pattern is based on a quadratic form and requires contours around the complex conjugate resonance frequencies ω_n^*, which are the poles of $\mathbf{E}^\circ(\omega)$, the circular contours in the upper half space can be ignored for the Purcell factor.

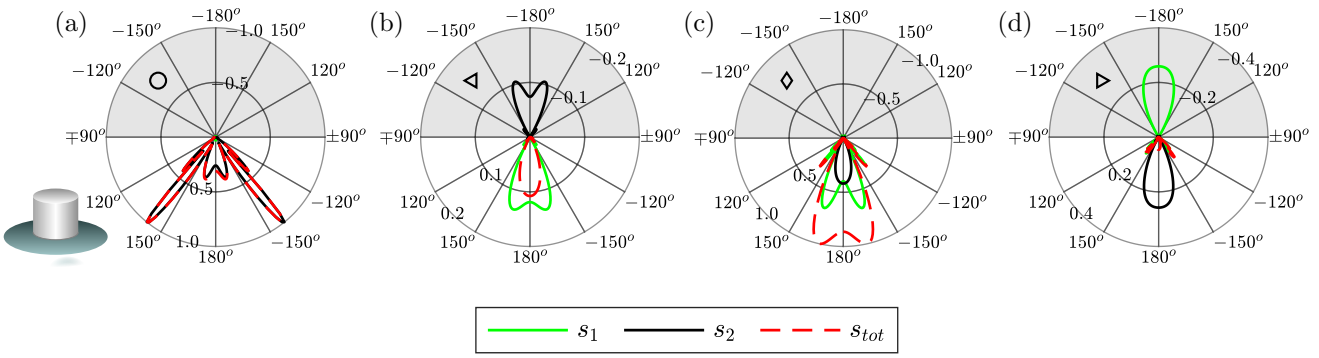

Figure 6. Modal analysis of the radiation pattern towards the substrate for a dipole located on the symmetry axis 27 nm below the upper base of the nanodisk. The black markers refer to Fig. 3 where they mark the corresponding wavelengths. The optimized system ($D/H = 0.92$) shown in (a) illustrates the dominance of a single mode. For (b)-(d) the aspect ratio is $D/H = 0.944$. Here, the radiation pattern results from the interference between two dominant modes. In (b), the pattern is shown at a wavelength blue shifted from the maximal Purcell enhancement, in (c), at the maximum and, in (d), at a red shifted wavelength.

with

$$\Gamma_n(\omega_0) = -\frac{1}{2\Gamma_b(\omega_0)} \oint_{C_n} \frac{\mathrm{Re}\left(\mathbf{E}(z,\mathbf{r}_d)\cdot\mathbf{j}^*(z,\mathbf{r}_d)\right)}{z-\omega_0} dz \quad \text{and}$$

$$\Gamma_{\text{background}}(\omega_0) = -\frac{1}{2\Gamma_b(\omega_0)} \oint_{C_{\text{background}}} \frac{\mathrm{Re}\left(\mathbf{E}(z,\mathbf{r}_d)\cdot\mathbf{j}^*(z,\mathbf{r}_d)\right)}{z-\omega_0} dz.$$

The contour C_n is the contour around the nth pole and $C_{\text{background}}$ is the large outer contour. Please refer to Fig. 5 and note that, for quantities linear in the electric field, such as the Purcell factor in the given form, the complex conjugate poles located in the upper half of the complex plane can be ignored. The integrals are computed numerically using the trapezoidal rule for the used circular and ellipsoidal contours.

In Section IV, we expand the far-field pattern of the radiated flux which is quadratic in the electric field, $s\left(\mathbf{E}(\omega),\mathbf{E}^*(\omega)\right) = \frac{1}{2}\,\mathrm{Re}\left(\mathbf{E}^*(\omega)\times\frac{1}{i\omega\mu_0}\nabla\times\mathbf{E}(\omega)\right)\cdot\mathbf{n}$, and hence involves its complex conjugate. The method for expanding quadratic forms was developed in [57]. The application of Cauchy's residue theorem requires a holomorphic expression and therefore does not allow for complex conjugation. As the electric field is a real quantity in the time domain, we have $\mathbf{E}^*(\omega) = \mathbf{E}(-\omega)$ for real ω. With the analytic continuation to the complex plane $\mathbf{E}^\circ(\omega)$ of $\mathbf{E}(-\omega)$, the holomorphic expression $s\left(\mathbf{E}(\omega),\mathbf{E}^\circ(\omega)\right) = \frac{1}{2}\,\mathrm{Re}\left(\mathbf{E}^\circ(\omega)\times\frac{1}{i\omega\mu_0}\nabla\times\mathbf{E}(\omega)\right)\cdot\mathbf{n}$ is defined. The poles of $\mathbf{E}^\circ(\omega)$ are located in the upper part of the complex plane. They are the complex conjugates of the resonance poles associated with $\mathbf{E}(\omega)$ as shown in Fig. 5. The expansion of $s\left(\mathbf{E}(\omega),\mathbf{E}^\circ(\omega)\right)$ consequently features resonant terms from poles in the lower and the upper part of the complex plane. Following this approach [57], one can derive the expansion of $s\left(\mathbf{E}(\omega),\mathbf{E}^\circ(\omega)\right)$,

$$s\left(\mathbf{E}(\omega_0),\mathbf{E}^\circ(\omega_0)\right) = -\sum_n \frac{1}{2i\pi}\oint_{C_n}\frac{s\left(\mathbf{E}(z),\mathbf{E}^\circ(z)\right)}{z-\omega_0}dz - \sum_n \frac{1}{2i\pi}\oint_{C_n^*}\frac{s\left(\mathbf{E}(z),\mathbf{E}^\circ(z)\right)}{z-\omega_0}dz + \frac{1}{2i\pi}\oint_{C_{\text{background}}}\frac{s\left(\mathbf{E}(z),\mathbf{E}^\circ(z)\right)}{z-\omega_0}dz,$$

where C_n is again the contour around the nth pole and $C_{\text{background}}$ is the large background contour. As mentioned above, we have to add the contours around poles in the upper part of the complex plane, which we denote by C_n^*. The expansion of the radiation pattern towards the air is discussed in Section IV. Here, for the sake of

completeness, we show the expansion of the radiation towards the substrate at the same wavelengths and aspect ratios as in Fig. 4. Overall, the same behavior is observed for the flux radiated towards the substrate as it was for the flux radiated towards the air. In Fig. 6(a), one can see that the modal contribution from the high-Q mode dominates all the other contributions. Figures 6(b-d) show once more that the radiation pattern of the flux results from the interference of the two main modes. In Figs. 6(b) and (d), they interfere destructively and, in Fig. 6(c), constructively.